Bioactive Materials 27 (2023) 337–347

Contents lists available at ScienceDirect

Bioactive Materials

journal homepage: www.keaipublishing.com/en/journals/bioactive-materials

A homologous and molecular dual-targeted biomimetic nanocarrier for EGFR-related non-small cell lung cancer therapy

Bin Xu [a,j,1], Fanjun Zeng [b,1], Jialong Deng [h,a,1], Lintong Yao [a,e], Shengbo Liu [d,a], Hengliang Hou [h,a], Yucheng Huang [i,a], Hongyuan Zhu [a], Shaowei Wu [d,a], Qiaxuan Li [a,e], Weijie Zhan [d,a], Hongrui Qiu [f,a], Huili Wang [f,a], Yundong Li [k], Xianzhu Yang [j], Ziyang Cao [g,j,**], Yu Zhang [c,*], Haiyu Zhou [a,d,e,f,h,i,***]

[a] *Department of Thoracic Surgery, Guangdong Provincial People's Hospital (Guangdong Academy of Medical Sciences), Southern Medical University, Guangzhou, 510080, PR China*
[b] *Department of General Practice, Guangdong Provincial Geriatrics Institute, Guangdong Provincial People's Hospital (Guangdong Academy of Medical Sciences), Southern Medical University, Guangzhou, 510080, PR China*
[c] *Department of Orthopedics, Guangdong Provincial People's Hospital (Guangdong Academy of Medical Sciences), Southern Medical University, Guangzhou, 510080, Guangdong, China*
[d] *The Second School of Clinical Medicine, Southern Medical University, Guangzhou, 510515, PR China*
[e] *Shantou University Medical College, Shantou, 515063, PR China*
[f] *Guangzhou University of Chinese Medicine, Guangzhou, 510006, PR China*
[g] *Guangzhou First People's Hospital, South China University of Technology, Guangzhou, 510006, PR China*
[h] *School of Biology and Biological Engineering, South China University of Technology, Guangzhou, 510006, PR China*
[i] *School of Medicine, South China University of Technology, Guangzhou, 510006, PR China*
[j] *School of Biomedical Sciences and Engineering, South China University of Technology, Guangzhou International Campus, Guangzhou, 511442, PR China*
[k] *South China Sea Fisheries Research Institute, Chinese Academy of Fishery Sciences, Key Laboratory of South China Sea Fishery Resources Exploitation and Utilization, Ministry of Agriculture and Rural Affairs, Guangzhou, 510300, China*

ARTICLE INFO

Keywords:
Biomimetic nanoparticles
Membrane targeting
EGFR mutation
Tyrosine kinase inhibitor
Intracellular drug delivery
Clinical efficacy
Non-small cell lung cancer

ABSTRACT

The abnormal activation of epidermal growth factor receptor (EGFR) drives the development of non-small cell lung cancer (NSCLC). The EGFR-targeting tyrosine kinase inhibitor osimertinib is frequently used to clinically treat NSCLC and exhibits marked efficacy in patients with NSCLC who have an EGFR mutation. However, free osimertinib administration exhibits an inadequate response in vivo, with only ~3% patients demonstrating a complete clinical response. Consequently, we designed a biomimetic nanoparticle ($CMNP^{@Osi}$) comprising a polymeric nanoparticle core and tumor cell-derived membrane-coated shell that combines membrane-mediated homologous and molecular targeting for targeted drug delivery, thereby supporting a dual-target strategy for enhancing osimertinib efficacy. After intravenous injection, $CMNP^{@Osi}$ accumulates at tumor sites and displays enhanced uptake into cancer cells based on homologous targeting. Osimertinib is subsequently released into the cytoplasm, where it suppresses the phosphorylation of upstream EGFR and the downstream AKT signaling pathway and inhibits the proliferation of NSCLC cells. Thus, this dual-targeting strategy using a biomimetic nanocarrier can enhance molecular-targeted drug delivery and improve clinical efficacy.

Peer review under responsibility of KeAi Communications Co., Ltd.
* Corresponding author.
** Corresponding author. Guangzhou First People's Hospital, South China University of Technology, Guangzhou, 510006, PR China.
*** Corresponding author. The Second School of Clinical Medicine, Southern Medical University, Guangzhou, 510515, PR China.
E-mail addresses: mccaozy@scut.edu.cn (Z. Cao), zhangyu@gdph.org.cn (Y. Zhang), zhouhaiyu@gdph.org.cn (H. Zhou).
[1] These authors contributed equally: Bin Xu, Fanjun Zeng, Jialong Deng.

https://doi.org/10.1016/j.bioactmat.2023.04.005
Received 10 October 2022; Received in revised form 30 March 2023; Accepted 4 April 2023

1. Introduction

Lung cancer is the first leading cause of cancer-related deaths in both men and women, with non-small cell lung cancer (NSCLC) responsible for the majority (~85% of the cases) [1]. Currently, conventional chemotherapy constitutes the mainstay of NSCLC treatment; however, its clinical efficacy remains limited. The low survival rate of patients with NSCLC has encouraged substantial research regarding alternative treatment strategies, such as molecular targeting [2]. Epidermal growth factor receptor (EGFR), a tyrosine kinase receptor, has been recognized as the most common driver for NSCLC [3–5]. Consequently, EGFR-targeting inhibitors, such as tyrosine kinase inhibitors (TKIs) (e.g., gefitinib and erlotinib), have been developed, and their clinical efficacy to treat advanced NSCLC has been confirmed, especially for lung adenocarcinoma (a subset of NSCLC) [6,7]. Upon binding to the EGFR tyrosine kinase domain, these small molecular inhibitors block EGFR phosphorylation, inhibit downstream signaling pathways and tumor proliferation [8]. However, the therapeutic effects of these small molecular inhibitors are usually compromised by intrinsic or acquired resistance, although TKIs considerably improve patient prognosis and prolong progression-free survival with few side effects [9].

Osimertinib (Osi) is a third-generation EGFR-TKI that was approved for treating patients with acquired resistance to first- or second-generation EGFR-TKIs. Osi exhibits marked efficacy for patients with NSCLC having EGFR mutations [10,11]. Indeed, in a few clinical NSCLC cases, Osi treatment extended progression-free survival compared with gefitinib or erlotinib treatment. Presently, Osi is considered a standard treatment for patients with NSCLC having EGFR mutations [12]. However, notably, a population of patients exhibited insufficient response to Osi treatment, similar to the responses observed for other EGFR-TKIs. Furthermore, most patients experienced recurrence and metastasis due to residual lesions, with only ~3% patients achieving complete remission [13]. The administration method of intravenous injection or oral ingestion (in a tablet formulation) constitutes the primary reason behind this insufficient response rate as they may lead to rapid blood/renal clearance, thereby causing low tumor accumulation and nonspecific distribution, resulting in an unsatisfactory treatment index and severe systemic toxicity [14,15]. Therefore, efforts to enhance drug enrichment at tumor sites and reduce systemic side effects are essential to increase the efficacy of Osi to clinically treat patients with NSCLC.

Among the various strategies for improving drug delivery and therapeutic efficacy, nanocarrier delivery exhibits several advantages for cancer therapy [16,17], including protecting the drug from biodegradation [18], adjusting drug distribution in vivo [19,20], reducing systemic toxicity [21,22], and improving therapeutic efficacy [23,24]. To date, more than a dozen nanomedicines have been approved for clinical use, including Doxil, Abraxanc, LipoDOX50, Onivyde, DepoCyt, Onpattro, and Apealea, which exhibit improved clinical profiles and efficacy [25]. More recently, drug-delivery strategies involving designs with membrane-coated biomimetic nanocarriers have demonstrated the potential to substantially enhance the functionality of the current nanoparticle platforms. This biomimetic design strategy derives inspiration from cellular membranes, which are essential for biointerfacing, self-identification, signal transduction, and compartmentalization, enabling the development of membrane-camouflaged nanocarriers with good biocompatibility and extended clearance times [26–29]. Moreover, membrane coating may endow nanocarriers with homotypic targeting capability, mediated by adhesion molecules expressed on the membrane, including integrin αvβ3 and tumor-specific binding proteins, such as Thomsen-Friedenreich antigen, E-cadherin, and Galectin-3. In addition, the endogenous cell membranes derived from autologous tumor cells might camouflage the exogenous chemically synthesized nanocarriers, thereby reducing their immunogenic responses. In addition, membrane proteins, including CD47, are beneficial for immune escape and prevent the macrophage recognition of membrane-coated nanocarriers. Hence, using cell membranes to functionalize nanocarrier surfaces is an extremely powerful design strategy to fabricate biomimetic nanocarriers that leverage natural processes that have evolved over eons, thereby circumventing the need for exhaustive discovery and validation that are often required for synthetic carriers [30].

However, bioinspired nanomedicine is still in its infancy and more effort is needed to explore novel biomimetic platforms to accelerate the commercialization and clinical application of nanoparticle-based drugs. The goal of membrane-coating technology is to create "next-generation" nanoparticle platforms that navigate and interact with complex biological systems and achieve enhanced and targeted drug delivery in vivo more effectively than the previous generation nanoparticle platforms. Such emerging technologies have the potential to considerably advance the field of nanomedicine, help improve traditional modalities, and enable novel applications. To promote clinical translation, the research priorities of bioinspired nanomedicine need to shift from discovery to close clinical integration. There are some challenges and safety issues should be addressed for further improvement cell membrane coating bioinspired nanocarriers. First, how to precisely characterize the integrity of cell membrane-camouflaged nanoparticles in vivo has not been uncovered, whose integrity is determining the functionality of bioinspired nanocarriers during blood circulation. Second, obstacles to the standard protocol, quality control and large-scale production also need to be overcome. Last, the long-term biological effects of cell membrane-camouflaged nanoparticles to living organisms require careful investigation. Especially, the biological safety of cancer cell membrane in the nanoparticles to the healthy organs should be investigated carefully since there are still a proportion of administrated cell membrane-camouflaged nanoparticles accumulated in healthy organs. Moreover, the safety concerns of this membrane-coating strategy mainly focus on immune response in vivo due to the immunogenicity of cell membranes deriving from various patients. Hence, for the future clinical translation, this strategy may become primarily an individualized treatment strategy for different patients. We believe that these important issues of cell membrane coating bioinspired nanocarriers will be further investigated in the near future.

Herein, we surface-functionalized Osi-loaded polymeric nanoparticles ($NP^{@Osi}$) using tumor cell membranes and obtained biomimetic nanoparticles ($CMNP^{@Osi}$) possessing in vivo dual targeting for antitumor therapy (Scheme 1). Furthermore, cancer cell membrane-camouflaged $CMNP^{@Osi}$ exhibited increased clearance time in vivo and homotypic targeting mediated by adhesion molecules and tumor-specific binding proteins closely resembling those of the source cancer cells. The $CMNP^{@Osi}$ also showed effective uptake by homologous cancer cells, subsequently releasing Osi into the cytoplasm, which bound to EGFR tyrosine kinase receptors on the interior membrane, enhancing molecular targeting and enabling efficient tumor growth inhibition. Thus, we presented a biomimetic nanocarrier strategy with combined homologous and molecular targeting for drug delivery to achieve dual targeting, which might expand the clinical application of cellular membrane-coating technology and improve its therapeutic efficacy.

2. Experimental methods

2.1. Materials

Osimertinib was purchased from Selleck Co. Ltd. (China). Dil was obtained from Thermo Fisher Scientific Inc. (USA). Coumarin 6 was procured from Sigma-Aldrich (USA). Antibodies, including Na–K-ATPase (3010), GADPH (5174), Histone H3 (4499), Galectin-3 (12733), CD44 (3570), and E-cadherin (5296) were purchased from Cell Signaling Technology (USA). The Cell Counting Kit-8 (CCK-8) reagent was obtained from Biosharp (China). Other chemicals and reagents were of analytical grade and used as received.

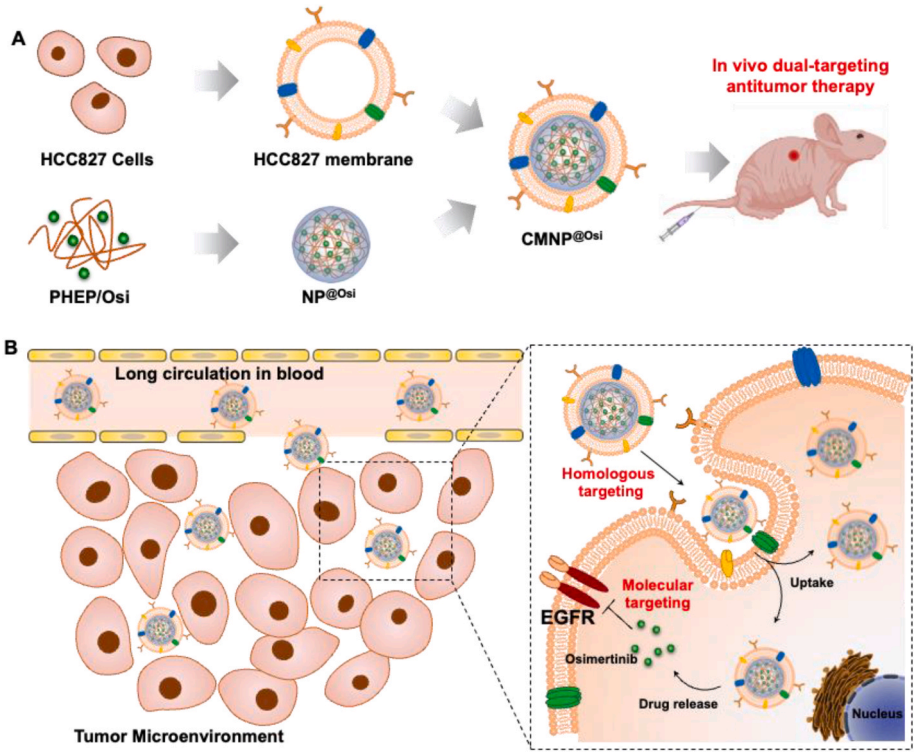

Scheme 1. Schematic showing the fabrication of biomimetic CMNP$^{@Osi}$ nanoparticles for HCC827 tumor therapy via tail vein injection (A) and homologous and molecular targeting therapy for tumors in vivo (B).

2.2. Cell lines and animals

HCC827, HFL1, LEWIS, MOVAS, and 293T cells were obtained from the American Type Culture Collection. The cells were cultured in RPMI 1640 or Dulbecco's Modified Eagle's Medium supplemented with 10% fetal bovine serum (FBS), 1% (v/v) penicillin, and 1% (v/v) streptomycin in an incubator at 37 °C and 5% CO_2 atmosphere. Female BALB/c nude mice (5 weeks old; weighing 18–22 g) were purchased from Hunan SJA Laboratory Animal Co., Ltd. All animal procedures were conducted according to the guidelines approved by the Care and Use of Laboratory Animals of the South China University of Technology.

2.3. Preparation of cancer cell membrane fragments

The cells were cultured in 100-mm petri dishes to full confluency, harvested using 2 mM ethylenediaminetetraacetic acid (Sigma-Aldrich) in phosphate-buffered saline (PBS, pH 7.4, Invitrogen), and washed with PBS thrice. The collected cells were subsequently suspended in hypotonic lysing buffer containing membrane protein extraction reagent and phenylmethanesulfonylfluoride (Beyotime). These cells were incubated on ice for 15 min and freeze-thawed seven times. The cell membrane debris and content were separated via first centrifugation at 700*g* for 15 min at 4 °C, and then the cell membrane fragments were obtained from the supernatant via centrifugation at 14,000 *g* for 30 min at 4 °C.

2.4. Synthesis of NP$^{@Osi}$ and CMNP$^{@Osi}$

Inner core polymeric polyphosphoester (PHEP) was synthesized as previously described [31,32]. Dimethyl sulfoxide (1 mL) containing 10 mg PHEP and 1 mg Osi (Selleck) were mixed and added dropwise to 10 mL deionized water under vigorous stirring for 2 h. The solution was then transferred to a dialysis bag with a 14K molecular weight cutoff and dialyzed against ultrapure water for 48 h. Free Osi was removed via filtering through a 0.45-μm filter to obtain NP$^{@Osi}$.

Subsequently, NP$^{@Osi}$ were surface-functionalized using the membrane fragments via filtering the latter through 400-nm polycarbonate porous membranes (Avanti) 11 times. The membranes were then mixed with NP$^{@Osi}$ and filtered through 200-nm polycarbonate porous membranes 11 times to obtain the biomimetic nanoparticles, CMNP$^{@Osi}$. Then, the standard curves of the free Osi solutions (0.625, 1.25, 2.5, 5, and 10 μg/mL) were prepared and the CMNP$^{@Osi}$ solution (100 μL) was freeze-dried and re-solve in 1 mL DMSO. After that, the absorbance of Osi standard curves and CMNP$^{@Osi}$ sample at 320 nm were determined by ultraviolet–vis spectrophotometer (Thermo Fisher, Evolution300, USA). Final, the Osi concentration in CMNP$^{@Osi}$ sample was direct calculated through the standard curve and the drug loading capacity (DLC) of Osi in CMNP$^{@Osi}$ was calculated as following equation, and is 5.37% ± 0.41%:

$$DLC\% = (M_{Osi}/M_{Nanocarrier}) \times 100\%$$

The M_{Osi} represented the total mass of encapsulated Osi in CMNP$^{@Osi}$ and the $M_{Nanocarrier}$ represented the total mass of CMNP$^{@Osi}$ consist of PHEP homopolymer.

2.5. Characterization of CMNP$^{@Osi}$

Dynamic light scattering (DLS) was performed using Zetasizer Nano ZSE (Malvern Instruments) at 25 °C to determine the size and zeta potential of HCC827 cell membranes, NP$^{@Osi}$, and CMNP$^{@Osi}$ dispersed in a diluted suspension. After staining with 1% (w/v) phosphotungstic acid, the morphologies of NP$^{@Osi}$ and CMNP$^{@Osi}$ were investigated via transmission electron microscopy (TEM, JEOL JEM-2010). In addition, the stability of CMNP$^{@Osi}$ was assessed by measuring size changes following incubation in 1 × PBS or PBS containing 10% FBS at 0, 6, 12, 24, 48 and 72 h.

Sodium dodecyl sulfate–polyacrylamide gel electrophoresis (SDS–PAGE) analysis was performed to analyze protein profiles after HCC827 cell lysis, including the separate assessment of cell membrane vesicles (CMV) and CMNP$^{@Osi}$. The proteins were stained with Coomassie blue (Invitrogen) and imaged after destaining in water overnight.

For western blotting, the proteins were transferred to polyvinylidene fluoride membranes (Millipore), which were then blocked and incubated with antibodies overnight at 4 °C. Next, secondary antibodies, including anti-mouse immunoglobulin G (IgG) (Cell Signaling Technology, 7076) and anti-rabbit IgG (Cell Signaling Technology, 7074), were coincubated with the corresponding primary antibodies. The images were collected using ECL western blotting substrate (Millipore).

The colocalization of the membranes and inner cores was observed using confocal laser scanning microscopy (CLSM). Dil (Invitrogen) was used to stain the cell membranes for 30 min, and coumarin 6 (MedChemExpress) was loaded into the hydrophobic cores of $CMNP^{@Osi}$. Dual fluorescence-labeled $CMNP^{@Osi}$ were coincubated with HCC827 cells for 2 h. After nucleus and cell membrane staining with Hoechst 33342 (Invitrogen, 1:1000 dilution) and CellMask Deep Red (Invitrogen, 1:1000 dilution) for 20 min, respectively, and then washing with PBS, the cells were observed by CLSM (Carl Zeiss, LSM880).

2.6. Cellular endocytic pathways

In order to study the cellular uptake mechanisms, three specific inhibitors were introduced to investigate the endocytic pathways of $CMNP^{@Osi}$ and $NP^{@Osi}$. HCC827 cells were incubated with various endocytic inhibitors, including chlorpromazine (10.0 μg/mL), amiloride (20.0 μg/mL), and carboxymethyl-β-cyclodextrin (5.0 mg/mL), and further incubated at 37 °C or 4 °C for 60 min, respectively. Subsequently, $CMNP^{@Osi}$ and $NP^{@Osi}$ were added and coincubated for 2 h, respectively. The cells were washed with PBS and collected for FACS analysis with an Accuri C6 flow cytometer.

2.7. In vitro homologous targeting study

The homologous targeting capacity of $CMNP^{@Osi}$ was investigated using fluorescence-activated cell sorting (FACS) and CLSM. The $CMNP^{@Osi}$ were labeled with coumarin 6 loaded into the hydrophobic inner core of the particles. Similar to the preparation of $CMNP^{@Osi}$, HFL1 cell membrane-coated $NP^{@Osi}$ (denoted as $FMNP^{@Osi}$) were prepared and used as a control. Next, $CMNP^{@Osi}$ and $FMNP^{@Osi}$ were coincubated with HCC827, HFL1, LEWIS, MOVAS, or 293T cells for 2 h. After trypsinization and washing with PBS, the cells were resuspended in PBS and intracellular fluorescence intensity was measured using FACS via a flow cytometer (Accuri C6). In addition, the HCC827 cells were coincubated with different formulations for 2 h and then collected for FACS and CLSM analyses. For CLSM, the cells were counterstained with Alexa Fluor546 phalloidin and DAPI (Carl Zeiss, LSM 880).

2.8. In vitro drug release study

$NP^{@Osi}$ and $CMNP^{@Osi}$ (1 mL, 35 μg/mL) loaded in dialysis bags (MW, 3500) were immersed in 20 mL of PB buffer (0.02 mM) and incubated at 37 °C. At pre-determined time points, 0.2 mL of the medium was drawn out and added with an equal volume of fresh medium. Then, the osimertinib concentration was determined using HPLC analysis.

2.9. In vitro antiproliferation and cell apoptosis assays

The in vitro antiproliferation assay used HCC827 cells seeded into 96-well plates at a density of 5×10^3 cells/well in 0.1 mL RPMI 1640 media with 10% FBS. After 24 h, the cells were incubated with fresh media containing free Osi, $NP^{@Osi}$, or $CMNP^{@Osi}$ with concentrations ranging from 2 to 64 nM. Following incubation for 72 h, cell viability was measured using the CCK-8 assay.

Following independent treatment with free Osi, $NP^{@Osi}$, or $CMNP^{@Osi}$ using 50 nM Osi, the HCC827 cells were assessed using Annexin V-FITC apoptosis detection kit (Beyotime) whose results were analyzed using FACS. The HCC827 cells treated with PBS were used as a negative control.

2.10. Cell migration assay

A wound-healing migration assay was performed to investigate the inhibition of cell migration of $CMNP^{@Osi}$. The HCC827 cells were incubated at 90%–100% confluence in the culture plate wells, and the media were replaced with serum-free media for 24 h. Then, three scratch lines were made using a 200-μL sterile micropipette tip, and the cells were washed twice with warm serum-free media. Subsequently, the cells were independently treated with free Osi, $NP^{@Osi}$, and $CMNP^{@Osi}$ using 50 nM Osi for 24 and 48 h. Finally, cell migration was imaged using a microscope (Nikon Eclipse Ti).

2.11. In vivo biodistribution and tumor homologous targeting

The distribution of $CMNP^{@Osi}$ in vivo was conjugated and labeled with Cy5.5 NHS ester and encapsulated in the hydrophobic core of $CMNP^{@Osi}$. Cy5.5-labeled $CMNP^{@Osi}$ was injected intravenously into HCC827 tumor-bearing mice and imaged using IVIS LuminaLT system (PerkinElmer) at different time points. At 48 h postinjection, the mice were euthanized to collect their primary organs and tumors for imaging. Cy5.5-labeled naked $NP^{@Osi}$ served as a control.

2.12. In vivo antitumor efficacy

Blbc/nude mice with HCC827 xenograft tumors (~50 mm^3) were randomly divided into four groups (n = 5/group). The mice were intravenously injected with PBS, free Osi, $NP^{@Osi}$, or $CMNP^{@Osi}$ using an Osi dose of 1.0 mg/kg every three days. The body weight and tumor size were monitored every three days. The mice were euthanized on day 21, and the tumor tissues were excised, weighed, and imaged. Further, the harvested tumor tissues were paraffin-embedded and sectioned for hematoxylin and eosin (H&E) and immunohistochemical (terminal deoxynucleotidyl transferase dUTP nick-end labeling [TUNEL] and ki67) staining. Moreover, portions of tumor tissue samples were homogenized and analyzed for total EGFR, phosphorylated EGFR, total AKT, and total phosphorylated AKT levels via western blotting. Finally, the tumor tissues from PBS- or $CMNP^{@Osi}$-treated mice were collected for mRNA sequencing.

2.13. In vivo pharmacokinetics

ICR mice were randomly grouped (n = 3 in each group) and injected intravenously with free osimertinib, $NP^{@Osi}$ and $CMNP^{@Osi}$, respectively, at the Osi dose of 1 mg/kg. At pre-determined time points, blood samples were collected from the retro-orbital plexus of the eye, and serum samples were obtained by centrifugation. Osimertinib in the serum was extracted with ethyl acetate and quantified using HPLC analysis.

2.14. Biocompatibility evaluation

Following treatment, the mice were euthanized and their whole blood was collected. Serum was obtained following centrifugation (14000 rpm, 10 min) for routine blood tests and biochemical examination. The histopathology of the organ tissues was assessed using paraffin sections following H&E staining.

2.15. Transcriptomic mRNA sequencing analysis

The tumor tissues from the mice following PBS or $CMNP^{@Osi}$ treatments were collected for mRNA sequencing. Fragments per kilobase of exon per million mapped fragment data were processed via data cleaning, quality control, and normalization to yield 17,796 annotated mRNA sequences. The differentially expressed genes (DEGs) were

identified using the limma package, with p-values of <0.05 and absolute values of fold change over a cutoff calculated as mean fold change plus two standard deviations.

Gene Ontology (GO), Kyoto Encyclopedia of Genes and Genomes (KEGG) pathways, and Gene Set Enrichment Analysis (GSEA) were used to identify the functional and pathway enrichment of DEGs using clusterProfiler package via R software. For GSEA analysis, the annotated gene sets "c2.all.v7.5.1.symbols.gmt," and "c6.all.v7.5.1.symbols.gmt" were downloaded from the Molecular Signatures Database. A protein–protein interaction network for DEGs was constructed via the connections retrieved from the STRING database and visualized using cytoHubba algorithm via Cytoscape software (Version 3.8.2). The gene functions in G2/M checkpoint, DNA damage repair, and apoptosis were obtained based on the "Hallmark gene sets" from the Molecular Signatures Database (Supplementary Table 1). The expression of the specific gene sets was compared and visualized using heatmap package via R software.

2.16. Statistical analysis

GraphPad Prism 8 was used for the data analyses. All values were expressed as mean ± SD (standard deviation). The differences between the groups were determined using two-tailed Student's t-tests and one-way analysis of variance. A p-value of <0.05 was considered statistically significant.

3. Results and discussion

3.1. Preparation and characterization of the biomimetic CMNP$^{@Osi}$

Firstly, the inner core NP$^{@Osi}$ particles were prepared with homopolymer PHEP and Osimertinib according to nanoprecipitation method (Fig. S1). DLS analysis revealed that the vesicles derived from the HCC827 cell membranes exhibited a hydrodynamic diameter of ~300 nm and that of the NP$^{@Osi}$ core was ~80 nm. Then, CMNP$^{@Osi}$ was obtained following the co-fusion of vesicles and NP$^{@Osi}$ and the size distribution of CMNP$^{@Osi}$ at different NP$^{@Osi}$ to membrane protein mass ratio were evaluated. As showed in Fig. S2, DLS analysis revealed that excess cell membrane is not conducive for particles preparation, and the CMNP$^{@Osi}$ exhibited a uniform particle size distribution at a lower mass ratio (NP/membrane fragments). Hence, we prepared CMNP$^{@Osi}$ at the ratio of NP/membrane protein is 1:0.0625 for the following experiments and the final diameter of the CMNP$^{@Osi}$ was ~100 nm (Fig. 1A). The obtained CMNP$^{@Osi}$ display a negative charge similar to that of membrane vesicles (Fig. 1B). This charge differs from that of naked NP$^{@Osi}$, thereby demonstrating the successful fabrication of biomimetic CMNP$^{@Osi}$.

The morphology of CMNP$^{@Osi}$ was examined via TEM; both naked NP$^{@Osi}$ and CMNP$^{@Osi}$ exhibited a spherical morphology. Conversely, membrane-coated CMNP$^{@Osi}$ demonstrated a distinct core-shell structure, and the coating membrane was visualized around the polymeric particles (Fig. 1C). Further, the proteins of CMNP$^{@Osi}$, HCC827 cell membranes, and raw cell lysates were analyzed via SDS-PAGE. The proteins were retained on the cell membranes and in CMNP$^{@Osi}$, even after hypotonic treatment and extrusion. Thus, the cell membrane proteins of the HCC827 cells were successfully transferred to CMNP$^{@Osi}$ (Fig. 1D).

Cell membrane-specific and intracellular representative proteins were further analyzed via western blotting. HCC827 cell lysates were rich in GAPDH, a cytoplasmic protein marker, and histone H3, a nuclear protein marker. Conversely, cell membrane vesicles (CMV) and CMNP$^{@Osi}$ displayed considerable enrichment of Na+/K + -ATPase, a

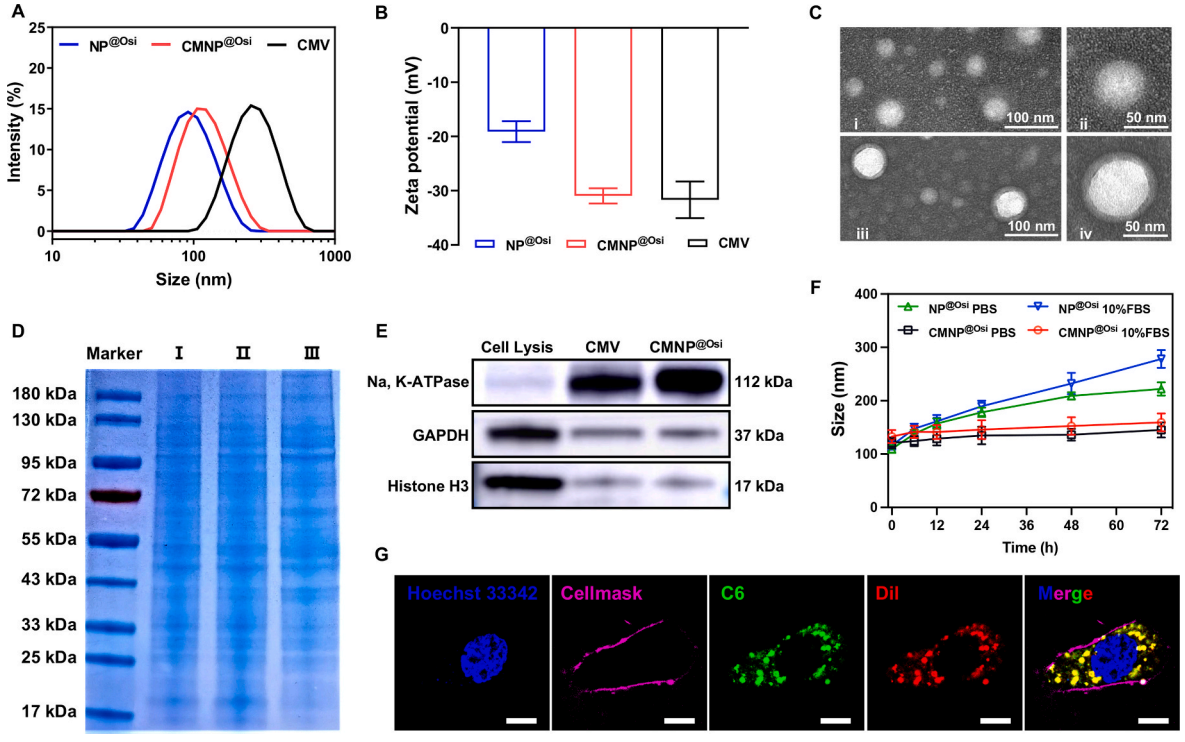

Fig. 1. Preparation and characterization of CMNP$^{@Osi}$. (A) Size and (B) zeta potential of NP$^{@Osi}$, CMNP$^{@Osi}$, and cell membrane vesicles (CMV). (C) Representative transmission electron microscopy images of (i, ii) naked NP$^{@Osi}$ and (iii, iv) CMNP$^{@Osi}$. (D) Sodium dodecyl sulfate-polyacrylamide gel electrophoresis protein marker analysis of (I) CMNP$^{@Osi}$, (II) CMV, and (III) HCC827 cell lysate. (E) Representative protein marker analysis of HCC827 cell lysate, CMV, and CMNP$^{@Osi}$ via western blotting assay, including GAPDH, histone H3, and Na+/K + -ATPase. (F) Time-dependent stability of CMNP$^{@Osi}$ or bared NP$^{@Osi}$ in 10% fetal bovine serum and phosphate-buffered saline solution. (G) Confocal laser scanning microscopy images of HCC827 cells coincubated with dual fluorescent dye-labeled CMNP$^{@Osi}$. Hoechst 33342: blue nuclei label, Cellmask Deep Red: light purple HCC827 cell membrane label, C6: green NP$^{@Osi}$ inner core label, Dil: red shell membrane label. Scale Bar: 10 μm.

plasma membrane marker, demonstrating the successful extraction of plasma membrane-associated proteins with negligible cytoplasmic/nuclear proteins (Fig. 1E). The plasma membrane coating imparts CMNP$^{@Osi}$ with good colloidal stability in PBS or 10% FBS (Fig. 1F), while the size of bared NP$^{@Osi}$ solution gradual increased along with prolong times under same condition. Moreover, the drug release curve revealed that Osi was gradually released from CMNP$^{@Osi}$ and NP$^{@Osi}$, indicating the Osimertinib release according to free diffusion and the membrane coating does not affect Osi release (Fig. S3). Furthermore, NP$^{@Osi}$ inner core and surface coating were labeled with coumarin 6 (C6) and Dil, respectively, and coincubated with HCC827 cells for 2 h. The intracellular distribution of CMNP$^{@Osi}$ after uptake was observed by CLSM (Fig. 1G). The fluorescence signals of the inner NP$^{@Osi}$ (green) and coating membrane (red) demonstrated intracellular excellent colocalization. Thus, CMNP$^{@Osi}$ was efficiently internalized by the homologous cancer cells while maintaining an intact core-shell structure.

3.2. Enhanced uptake of CMNP$^{@Osi}$ in vitro via homologous targeting

The homotypic targeting of CMNP$^{@Osi}$ was assessed via the analysis of primary surface adhesion molecules, including Galectin-3, E-cadherin, and CD44, using western blotting. All proteins were enriched in purified HCC827 membrane vesicles and CMNP$^{@Osi}$, indicating that three representative homotypic cell adhesion proteins were successfully transferred to the shell of CMNP$^{@Osi}$. Further, the HCC827 cells were coincubated with different particle formulations. After 2 h of incubation, the HCC827 cells were analyzed using FACS. The HCC827 cells coincubated with CMNP$^{@Osi}$ exhibited 2.1-fold and 1.9-fold higher intracellular fluorescence (Fig. 2B and C) than that exhibited with NP$^{@Osi}$ and FMNP$^{@Osi}$ (negative control, HCC827 cells replaced with HFL1 cells membrane-coated NP$^{@Osi}$) treatment, respectively. Similarly, increased fluorescence (C6) was observed in the CLSM images of the HCC827 cells, demonstrating a higher uptake of homotypic-coated nanoparticles (CMNP$^{@Osi}$) than heterotypic FMNP$^{@Osi}$ (Fig. 2D). In addidtion, the endocytosis mechanism study indicated that the cellular uptake of CMNP$^{@Osi}$ mainly through clathrin-dependent endocytosis and is an energy-dependent process (Fig. S4). Hence, homotypic targeting was concluded to be specific for homogeneous membranes.

Further, CMNP$^{@Osi}$ uptake by various cell types was investigated using FACS. Compared with naked NP$^{@Osi}$, intracellular FACS fluorescence and mean fluorescence intensity (MFI) following CMNP$^{@Osi}$ treatment of HCC822 cells was significantly increased. However, negligible differences were observed following the treatment of heterotypic cells, including HFL1, LEWIS, MOVAS or 293T cells (Fig. 2E and F). Thus, CMNP$^{@Osi}$ displays better affinity toward its homotypic cells. The superior targeting to homologous cancer cells of CMNP$^{@Osi}$ may be driven by the adhesive molecules in the homotypic membranes.

3.3. CMNP$^{@Osi}$ delivery of Osi significantly improved molecular targeting in vitro

CCK-8 assays were performed to assess the antiproliferation effects of CMNP$^{@Osi}$ in HCC827 cells. CMNP$^{@Osi}$ exhibited the best efficacy and the lowest half maximal inhibitory concentration (IC_{50}) of 14.23 nM. The calculated IC_{50} of free Osi and NP$^{@Osi}$ were 37.60 and 27.86 nM, respectively (Fig. 3A). We hypothesized that the homologous targeting of CMNP$^{@Osi}$ increased the cellular uptake. Moreover, the antitumor effects of different formulations were evaluated for apoptosis (Fig. 3B and C). CMNP@^{Osi} induced the most pronounced effect (52.87%), 3.56- and 4.20-fold higher than that of NP@^{Osi} and free Osi. Notably, the CMNP$^{@Osi}$ also could efficiently kill tumor cells at acidic environment (Fig. S5). Next, the antiproliferation activity of CMNP$^{@Osi}$ was also

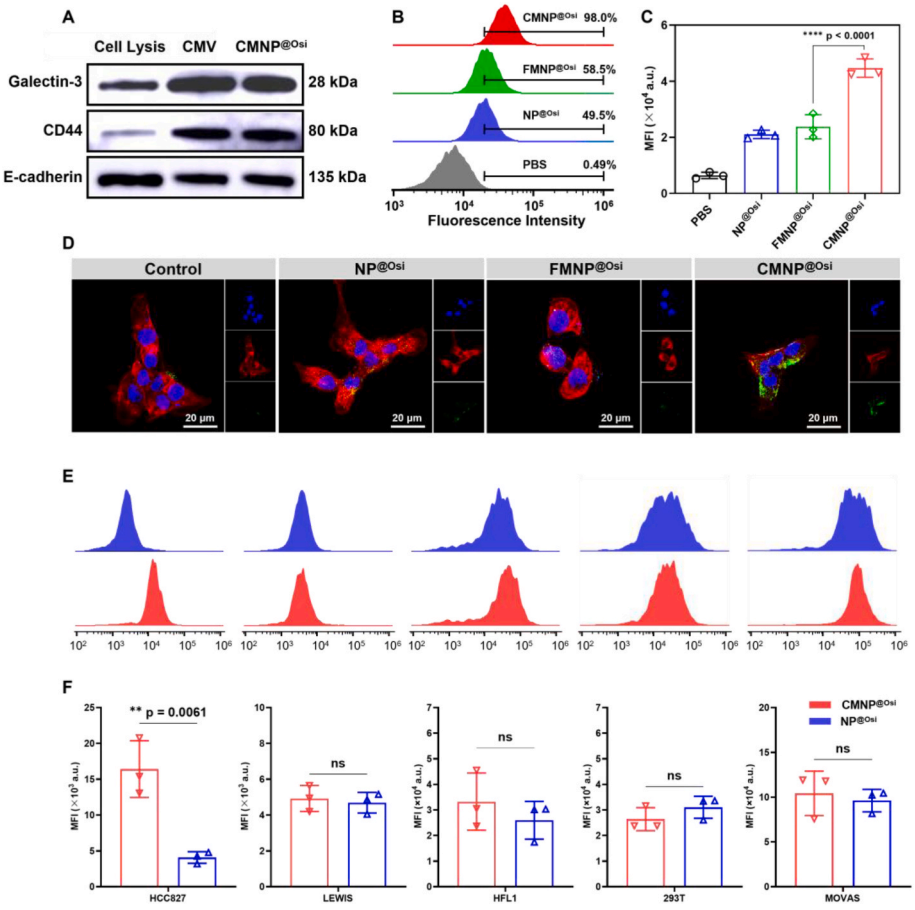

Fig. 2. In vitro cellular uptake and specific homologous targeting capacity of CMNP$^{@Osi}$. (A) Membrane protein analysis of the raw HCC827 cell lysate, cell membrane vesicles (CMV) and CMNP$^{@Osi}$ via western blotting. (B) Fluorescence-activated cell sorting (FACS) analysis and (C) mean fluorescence intensity (MFI) of the HCC827 cells incubated with different particle formulations, including PBS, NP$^{@Osi}$, FMNP$^{@Osi}$, or CMNP$^{@Osi}$. Data are means ± s.d. (n = 3). (D) Representative confocal laser scanning microscopy images of the HCC827 cells coincubated with different particle formulations (green). The nuclei were stained with DAPI (blue) and the actin cytoskeleton with Alexa Fluor™ 546 (red). (E) FACS analysis and (F) MFI of cells incubated with NP$^{@Osi}$ and CMNP$^{@Osi}$. Data are means ± s.d. (n = 3). Statistical significance was calculated via Student's t-test (two-tails), *p < 0.05, **p < 0.01, ***p < 0.001, and ****p < 0.0001. ns: no significant difference.

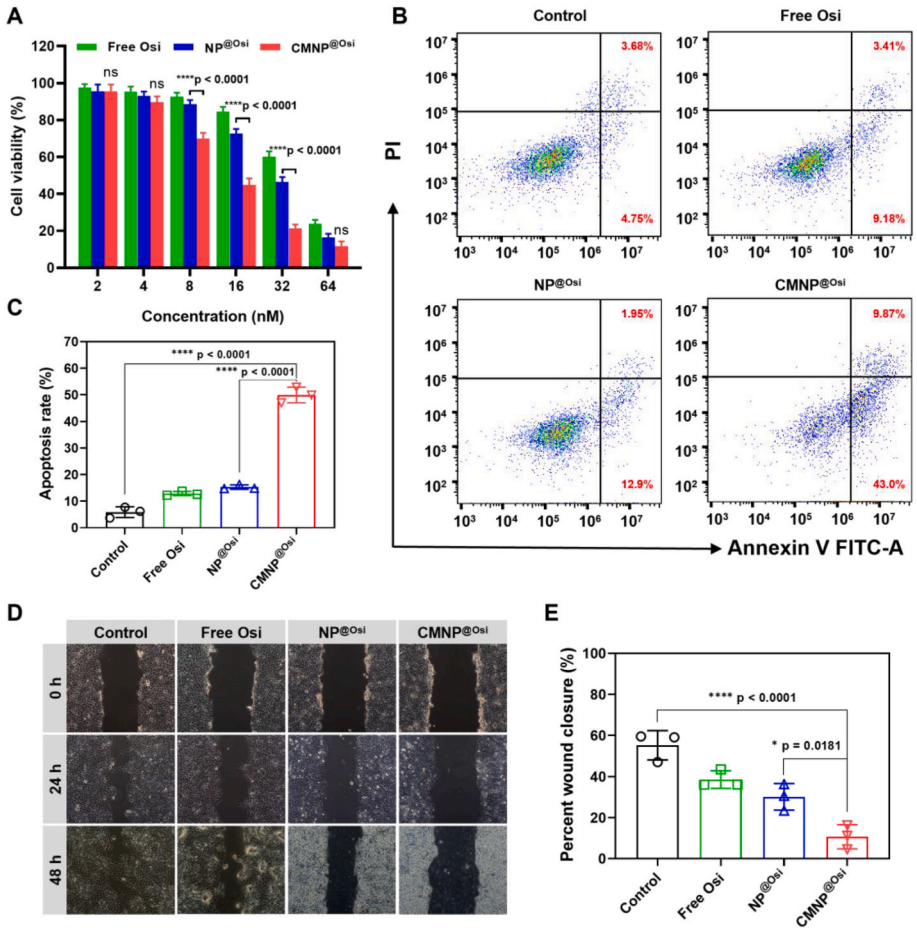

Fig. 3. In vitro efficacy of different formulations in HCC827. (A) Cytotoxicity of free Osi, NP$^{@Osi}$, and CMNP$^{@Osi}$ toward HCC827 cells after 72 h. (B) Fluorescence-activated cell sorting analysis and (C) quantification of apoptosis induced by different formulations. Data are means ± s.d. (n = 3). (D) Scratch assay and (E) quantification of cell migration after treatment with different formulations. Data are means ± s.d. (n = 3). Statistical significance was calculated via Student's t-test (two-tails), *p < 0.05, **p < 0.01, ***p < 0.001, and ****p < 0.0001. ns: no significant difference.

evident in the results of the wound-healing assays. The cell migration rate following CMNP$^{@Osi}$ treatment remained at ~10.68% at 48 h. Conversely, the cell migration rate in the cells treated with control, free Osi, and NP$^{@Osi}$ were 55.21%, 38.54%, and 30.11%, respectively. Thus, CMNP$^{@Osi}$ significantly inhibited the migration and proliferation of HCC827 cells (Fig. 3D–E). Thus, the homologous membrane-coating functionalization significantly improved the potential antitumor activity of nanoparticles in vitro owing to its superior targeting to homologous cancer cells.

3.4. *Homologous targeting of biomimetic nanoparticles CMNP$^{@Osi}$ accumulated in tumor tissues and their superior therapeutic efficacy*

We further investigated the distribution of biomimetic CMNP$^{@Osi}$ in vivo. The mice were imaged using Xenogen IVIS Lumina system following the intravenous administration of Cy5.5-labeled CMNP$^{@Osi}$ or naked NP$^{@Osi}$. Cy5.5 fluorescence intensity reached maxima at 6 h at the tumor sites following CMNP$^{@Osi}$ or NP$^{@Osi}$ treatment. However, the fluorescence signals following CMNP$^{@Osi}$ treatment was significantly stronger than those following naked NP$^{@Osi}$ treatment (Fig. 4A).

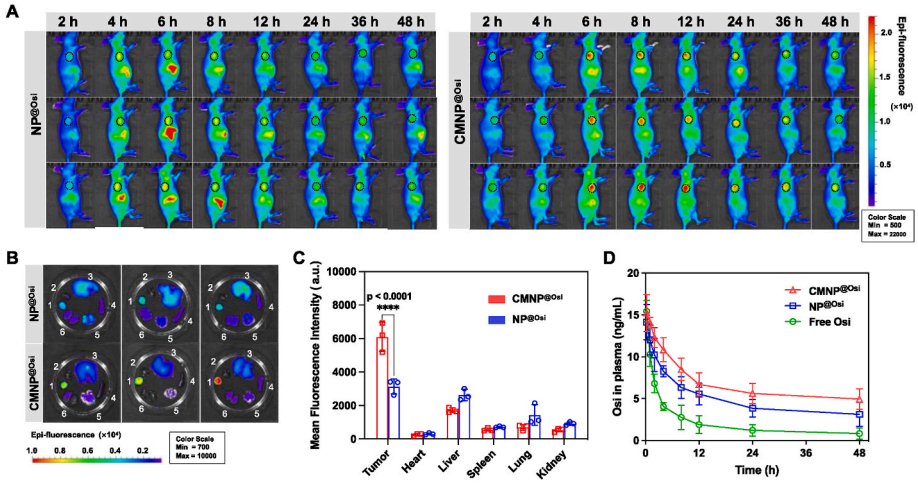

Fig. 4. In vivo homologous targeting and distribution of CMNP$^{@Osi}$. (A) Distribution of NP$^{@Osi}$ and CMNP$^{@Osi}$ in nude mice bearing HCC827 xenograft tumors imaged at different postinjection times. (B) Distribution and (C) quantitation of Cy5.5 fluorescence signals in the main organs and tumors. (1) Tumor, (2) heart, (3) liver, (4) spleen, (5) lungs, and (6) kidneys. Data are means ± s.d. (n = 3). (D) In vivo Osimertinib plasma concentration-time profile of free Osi, NP$^{@Osi}$ and CMNP$^{@Osi}$ after intravenous administration to mice (n = 3). Statistical significance was calculated via Student's t-test (two-tails), *p < 0.05, **p < 0.01, ***p < 0.001, and ****p < 0.0001.

Subsequently, the higher Cy5.5 fluorescence following CMNP$^{@Osi}$ treatment was sustained at the tumor sites up to 48 h after the injection. The major organs and tumor tissues were separated and imaged 48 h following the injection. The mice treated with CMNP$^{@Osi}$ displayed stronger Cy5.5 fluorescence in tumor tissues, indicating that the membrane-coated particles had accumulated in the tumors (Fig. 4B, the raw images were showed in Fig. S7). Notably, the fluorescence signals were weaker in the major organs than in the tumors, including the heart, liver, spleen, lungs, and kidneys, reflecting effective targeting and suggesting less systemic toxicity in vivo. Moreover, the quantitation of fluorescence signals in the tumor tissues showed that CMNP$^{@Osi}$ group exhibited 1.9-fold higher signals than that of NP$^{@Osi}$ (Fig. 4C). Additionally, the pharmacokinetics of free Osi, NP$^{@Osi}$ and CMNP$^{@Osi}$ were also determined. In comparison to free Osi and NP$^{@Osi}$, CMNP$^{@Osi}$ efficiently prolonged circulation (Fig. 4D) and the pharmacokinetic parameters were calculated (Table S1). It suggested that endogenous tumor cells membrane coating could reduce the elimination by reticuloendothelial system and enhance blood retention of biomimetic nanoparticles.

The anticancer activity of CMNP$^{@Osi}$ in vivo was evaluated in HCC827 xenograft tumor-bearing blab/c nude mice. The mice were randomly categorized into four groups (n = 5/group) and intravenously injected with PBS, free Osi, NP$^{@Osi}$, or CMNP$^{@Osi}$ at an Osi dose of 1.0 mg/kg every three days. The tumor size was monitored across the entire treatment period. The tumor growth curves revealed a superior efficacy of CMNP$^{@Osi}$ compared with that of either naked NP$^{@Osi}$ or free Osi (Fig. 5A–C; Fig. S6). In particular, tumor growth was almost completely suppressed following CMNP$^{@Osi}$ treatment. Subsequently, H&E and immunofluorescence staining (Ki-67 and TUNEL) of the tumor tissues revealed enhanced tumor cell apoptosis or necrosis and reduced proliferation following CMNP$^{@Osi}$ treatment (Fig. 5D, the raw images were showed in Fig. S8). Moreover, the body weight of mice did not show apparent change during the treatments regardless of which formulation was used (Fig. 5E). This finding suggests the favorable biocompatibility of CMNP$^{@Osi}$. The negligible alterations in the results of the routine blood tests and lack of significant histopathology in the major organs were consistent with this finding of in vivo biocompatibility (Figs. S9–10).

We also explored the phosphorylation status of EGFR and downstream AKT proteins following CMNP$^{@Osi}$ treatment. Western blotting revealed little or no effect of CMNP$^{@Osi}$ treatment on the protein expression of EGFR and AKT compared with that of NP$^{@Osi}$ and free Osi. However, the phosphorylation levels of EGFR and AKT proteins were significantly decreased following CMNP$^{@Osi}$ treatment (Fig. 5F). Moreover, CMNP$^{@Osi}$ treatment produced the lowest ratio of phosphorylated to nonphosphorylated EGFR and AKT proteins (Fig. 5G and H). Hence, CMNP$^{@Osi}$ enhanced the molecular targeting and anticancer activity of Osi.

3.5. Tumor mRNA analysis

The pathways and mechanisms of CMNP$^{@Osi}$ action in vivo were assessed using mRNA sequences following CMNP$^{@Osi}$ or PBS treatment. In total, 17,796 genes were analyzed. The differential expression of 466

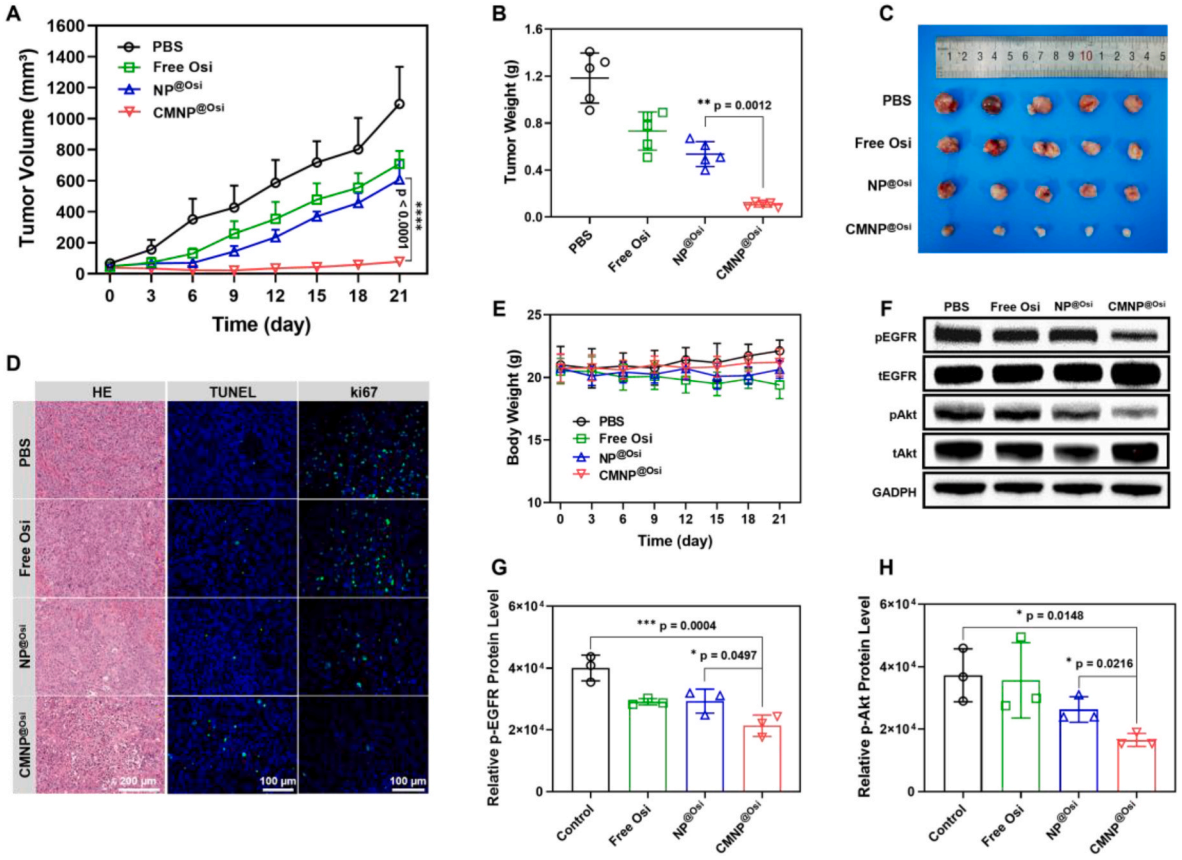

Fig. 5. Antitumor and antiproliferation activities of biomimetic CMNP$^{@Osi}$ in vivo. (A) Growth curves of HCC827 xenograft tumors and (B) tumor weights following different treatments for 21 days. (C) Images of tumor tissues following treatment. (D) Representative images of hematoxylin and eosin staining and immunofluorescence of terminal deoxynucleotidyl transferase dUTP nick-end labeling and Ki67 in tumor sections following treatments. (E) Mouse body weight curves over 21 days of treatment. Representative immunoblotting images (F) and quantitative relative phosphorylated-epidermal growth factor receptor (G) and p-AKT (H) protein levels via western blotting. Data are means ± s.d. (n = 3). Statistical significance was calculated via Student's t-test (two-tails), *p < 0.05, **p < 0.01, ***p < 0.001, and ****p < 0.0001.

genes was recognized using the criteria of fold change of ≥2-fold of mean fold change plus two standard deviations, $\log_2$ |fold change| ≥0.80 and $p < 0.05$; 310 DEGs were upregulated and 156 were downregulated (Fig. 6A). KEGG pathway analysis (Fig. 6B) further revealed the correlated pathways of the DEGs that were simultaneously involved in mTOR signaling, cell cycle, Ras signaling, apoptosis, and Foxo signaling. GO annotation functional analysis (Fig. 6C) suggested that the DEGs were associated with intrinsic apoptotic signaling, cell cycle G2/M phase transition, cell growth regulation, G2/M transition of the mitotic cell cycle, and apoptotic signaling regulation of processes that regulate GTPase regulator activity, cadherin binding, transcription coregulator activity, and transcription coactivator activity of molecular function. The possible associations with apoptosis, cell cycle G2/M phase transition, and transcription were notable following CMNP$^{@Osi}$ treatment. Further, GSEA confirmed the overexpression of oncogenic genes *EGFRM*, *ERBB2*, *MEK*, *mTOR*, and *PTEN* in EGFR-related HCC827 tumors (Fig. 6D). The tumor cells were arrested at G2/M of the cell cycle and exhibited negligible downregulation of apoptosis and the hedgehog pathways (Fig. 6E).

The downstream regulation and relevant proteins in the tumor tissue following CMNP$^{@Osi}$ treatment were explored using protein–protein interactions (Fig. 7A and B). The hub genes *RPA1*, *ATR*, *KAT5*, *MDC1*, *XRCC3*, and *UBB* were upregulated and *CXCL1*, *IL1A*, *IL6*, *MMP9*, and *SPRR1B* were downregulated following CMNP$^{@Osi}$ treatment. These genes participate in G2/M checkpoint, DNA damage repair, and apoptosis. Notably, *ATR* is sensitive to double-strand DNA breakage that causes G2 cell cycle arrest and induces apoptosis in aberrantly replicating cells. *MDC1* is also a critical tumor suppressor gene involved in DNA damage repair [33–35]. These genes were upregulated following CMNP$^{@Osi}$ treatment and may prevent cell proliferation by inhibiting the replication of malignant cells, thereby interfering with carcinogenesis. Moreover, increased G2/M arrest might induce apoptosis in stressed tumor cells. Next, we used our heatmap to identify differences in gene expression between CMNP$^{@Osi}$ and PBS treatments. Translation-related genes were downregulated and G2/M cell cycle–related genes were significantly upregulated following CMNP$^{@Osi}$ treatment (Fig. 7C and D). Overall, CMNP$^{@Osi}$ treatment induced the arrest EGFR-related cancer cells at the G2/M phase, upregulated tumor suppressor genes, and induced cell apoptosis by inhibiting cell replication, thereby improving cancer therapy efficacy.

4. Conclusion

Compared with other bioinspired nanoparticles, such as protein and glycans along with their derivatives-modified nanoparticles, the use of natural cell membranes to directly fabricate nanocarriers or as coating materials for synthetic nanoparticulate cores is convenient and less expensive. The membranes may endow the nanoparticles with cell-like

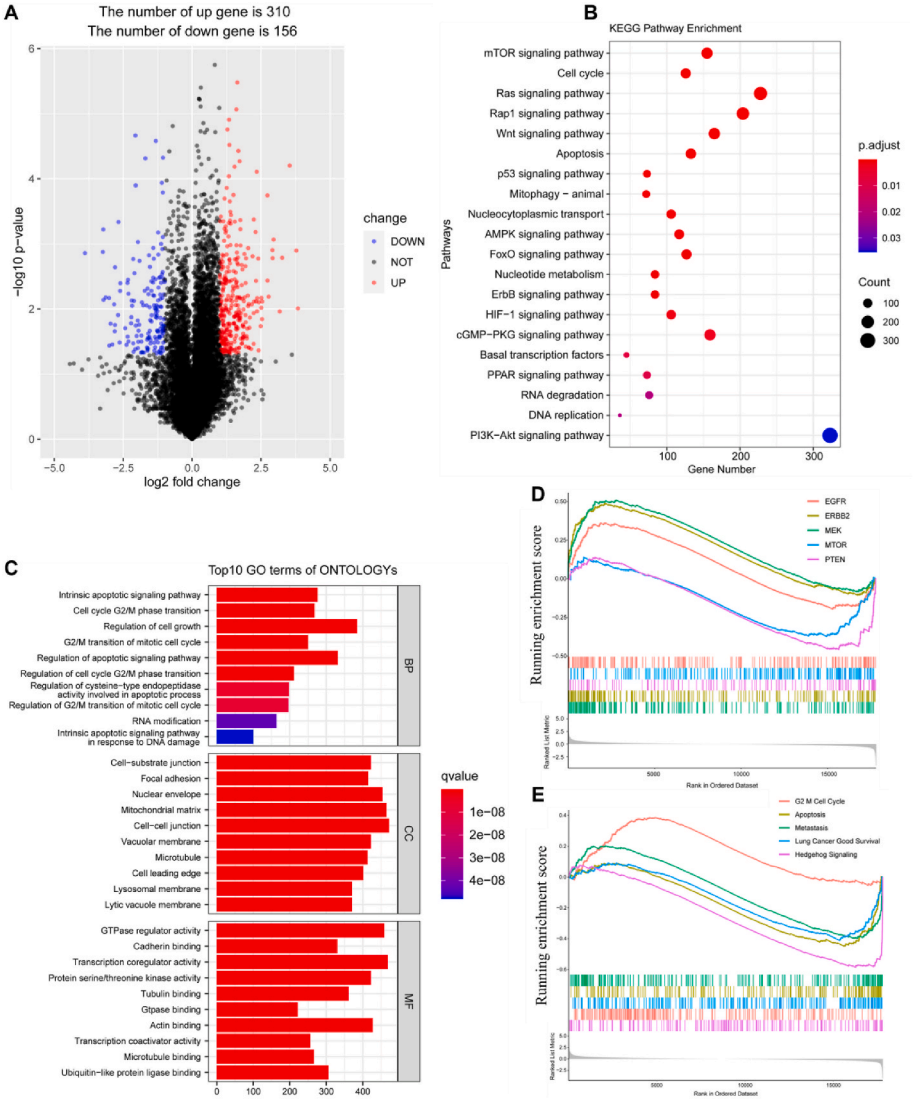

Fig. 6. mRNA sequence analysis. (A) Volcano plot of gene expression of upregulated (310) and downregulated (156) genes ($\log_2$ |fold change| ≥ 0.80 and $p < 0.05$) following CMNP$^{@Osi}$ treatment. (B) Kyoto Encyclopedia of Genes and Genomes pathway and (C) GO annotation analysis of the differentially expressed genes. (D) Gene Set Enrichment Analysis (GSEA) of the oncogene signature for epidermal growth factor receptor-related genes. (E) GSEA of G2/M checkpoint and apoptosis in tumor cells following CMNP$^{@Osi}$ treatment in the canonical curated pathways.

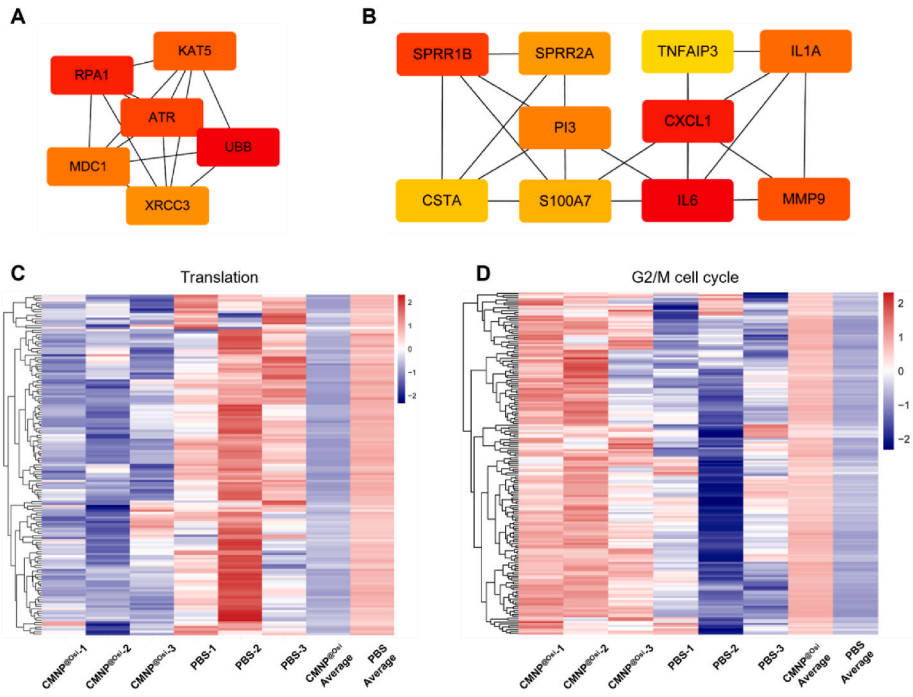

Fig. 7. Downstream gene expression analysis. Protein–protein interaction network of (A) upregulated and (B) downregulated genes constructed using cytoHubba algorithm via Cytoscape software. The heatmap of downregulated translation-related genes (C) and upregulated G2/M cell cycle–related genes (D) following CMNP$^{@Osi}$ or PBS treatments.

biological functions. We successfully developed a biomimetic nanocarrier CMNP$^{@Osi}$ with homologous targeting, drawing on previously reported designs for cell membrane-coated nanocarriers. We focused on the clinical applications of bioinspired nanoparticles for tumor therapy and demonstrated improved molecular targeting of Osi. Intravenously administered CMNP$^{@Osi}$ preferentially accumulated in tumor tissues and demonstrated enhanced uptake into cancer cells mediated by surface adhesion molecules and tumor-specific binding proteins, including Galectin-3, E-cadherin and CD44. Subsequently, CMNP$^{@Osi}$ released the tyrosine kinase inhibitor, Osi, into the cytoplasm, which suppressed the phosphorylation of EGFR and the key downstream protein AKT, which cis crucial for the proliferation of NSCLC cells. Biomimetic CMNP$^{@Osi}$ efficiently inhibited the proliferation of homologous HCC827 tumor cells and tissues both in vitro and in vivo. In addition, CMNP$^{@Osi}$ induced EGFR-related cancer cell arrest at the G2/M phase, upregulated tumor suppressor genes, and activated cell apoptosis. Notably, biomimetic particles substantially enhanced responses to Osi in vivo and achieved complete inhibition of EGFR-related NSCLC tumor proliferation. Compare with previously reported bionic nanocarriers, our study developed a customized molecular targeting strategy that combines homologous- and molecular drug-targeting, thereby rendering the strategy dual targeting and encouraging its clinical implementation and the applications of cellular membrane-coating technology.

However, there still is a weakness in vivo model of this study, only a subcutaneous tumor model was established for investigating the efficacy of CMNP$^{@Osi}$. Subcutaneous tumor model acted as an important tumor model in preclinical research because of short establishment cycle, high rate of tumor formation, easy operation and low cost. Notably, the in vivo tumor models which are close to pathophysiological situation (eg. Orthotropic cancer) are indispensable to further demonstrate the efficacy of our strategy. Hence, priority will give to the construction of orthotropic tumor models for study is important in future study works.

Based on our results, homologous targeting might also be achieved in other types of cancer cells. Moreover, a shift in focus from bioinspired discovery to process development and integration with clinical needs will be required as methods and workflows are developed for the reliable scaling up of fabrication and solutions for clinical problems. Overall, studies will continue to explore biomimetic design, and bioinspired nanomedicine may drastically alter the landscape of nanomedicine.

Declaration of competing interest

The authors declare no conflict of interest.

CRediT authorship contribution statement

Bin Xu: Conceptualization, Methodology, Investigation, Writing – original draft, Writing – review & editing. **Fanjun Zeng:** Writing – original draft, Methodology, experimental design. **Jialong Deng:** Cell experiments, Investigation, Validation. **Lintong Yao:** Writing – original draft, Transcriptomic analysis. **Shengbo Liu:** Writing – original draft, Investigation. **Hengliang Hou:** Animal experiments, Supplement experiment. **Yucheng Huang:** Animal experiments, Supplement experiment. **Hongyuan Zhu:** Methodology, Investigation. **Shaowei Wu:** Investigation. **Qiaxuan Li:** Investigation. **Weijie Zhan:** Validation. **Hongrui Qiu:** Validation. **Huili Wang:** Validation. **Yundong Li:** Validation. **Xianzhu Yang:** Writing – review & editing. **Ziyang Cao:** Formal analysis, Writing – review & editing, Funding acquisition. **Yu Zhang:** Writing – review & editing, Funding acquisition. **Haiyu Zhou:** Supervision, Project administration, Writing – review & editing, Funding acquisition.

Acknowledgments

This work was supported by the National Key R&D Program of China (No. 2022YFD2401900), the National Natural Science Foundation of China (No. 52203163), the High-level Hospital Construction Project (No. DFJH201905), the Natural Science Foundation of Guangdong (No. 2021A1515010838), the International Science and Technology Cooperation Program of Guangdong (No. 2022A0505050048), the Science and Technology Program of Guangzhou (No. 201903010028), Guangdong Provincial People's Hospital Intermural Program (No.

KJ012019447).

Appendix A. Supplementary data

Supplementary data to this article can be found online at https://doi.org/10.1016/j.bioactmat.2023.04.005.

References

[1] R.L. Siegel, K.D. Miller, H.E. Fuchs, A. Jemal, Cancer statistics, CA-Cancer J. Clin. 72 (1) (2022) 7–33.

[2] F.R. Hirsch, G.V. Scagliotti, J.L. Mulshine, R. Kwon, W.J. Curran Jr., Y.L. Wu, L. Paz-Ares, Lung cancer: current therapies and new targeted treatments, Lancet 389 (10066) (2017 Jan 21) 299–311.

[3] J. Xu, C. Zhang, X. Wang, L. Zhai, Y. Ma, Y. Mao, K. Qian, C. Sun, Z. Liu, S. Jiang, M. Wang, L. Feng, L. Zhao, P. Liu, B. Wang, X. Zhao, H. Xie, X. Yang, L. Zhao, Y. Chang, J. Jia, X. Wang, Y. Zhang, Y. Wang, Y. Yang, Z. Wu, L. Yang, B. Liu, T. Zhao, S. Ren, A. Sun, Y. Zhao, W. Ying, F. Wang, G. Wang, Y. Zhang, S. Cheng, J. Qin, X. Qian, Y. Wang, J. Li, F. He, T. Xiao, M. Tan, Integrative proteomic characterization of human lung adenocarcinoma, Cell 182 (1) (2020) 245–261.

[4] M. Jamal-Hanjani, G.A. Wilson, N. McGranahan, N.J. Birkbak, T.B.K. Watkins, S. Veeriah, S. Shafi, D.H. Johnson, R. Mitter, R. Rosenthal, M. Salm, S. Horswell, M. Escudero, N. Matthews, A. Rowan, T. Chambers, D.A. Moore, S. Turajlic, H. Xu, S.M. Lee, M.D. Forster, T. Ahmad, C.T. Hiley, C. Abbosh, M. Falzon, E. Borg, T. Marafioti, D. Lawrence, M. Hayward, S. Kolvekar, N. Panagiotopoulos, S. M. Janes, R. Thakrar, A. Ahmed, F. Blackhall, Y. Summers, R. Shah, L. Joseph, A. M. Quinn, P.A. Crosbie, B. Naidu, G. Middleton, G. Langman, S. Trotter, M. Nicolson, H. Remmen, K. Kerr, M. Chetty, L. Gomersall, D.A. Fennell, A. Nakas, S. Rathinam, G. Anand, S. Khan, P. Russell, V. Ezhil, B. Ismail, M. Irvin-Sellers, V. Prakash, J.F. Lester, M. Kornaszewska, R. Attanoos, H. Adams, H. Davies, S. Dentro, P. Taniere, B. O'Sullivan, H.L. Lowe, J.A. Hartley, N. Iles, H. Bell, Y. Ngai, J.A. Shaw, J. Herrero, Z. Szallasi, R.F. Schwarz, A. Stewart, S.A. Quezada, J. Le Quesne, P. Van Loo, C. Dive, A. Hackshaw, C. Swanton, TRACERx consortium, tracking the evolution of non-small-cell lung cancer, N. Engl. J. Med. 376 (22) (2017) 2109–2121.

[5] Cancer Genome Atlas Research Network, Comprehensive molecular profiling of lung adenocarcinoma, Nature 511 (7511) (2014) 543.

[6] J.G. Paez, P.A. Jänne, J.C. Lee, S. Tracy, H. Greulich, S. Gabriel, P. Herman, F. J. Kaye, N. Lindeman, T.J. Boggon, K. Naoki, H. Sasaki, Y. Fujii, M.J. Eck, W. R. Sellers, B.E. Johnson, M. Meyerson, EGFR mutations in lung cancer: correlation with clinical response to gefitinib therapy, Science 304 (5676) (2004) 1497–1500.

[7] T.J. Lynch, D.W. Bell, R. Sordella, S. Gurubhagavatula, R.A. Okimoto, B. W. Brannigan, P.L. Harris, S.M. Haserlat, J.G. Supko, F.G. Haluska, D.N. Louis, D. C. Christiani, J. Settleman, D.A. Haber, Activating mutations in the epidermal growth factor receptor underlying responsiveness of non-small-cell lung cancer to gefitinib, N. Engl. J. Med. 350 (21) (2004) 2129–2139.

[8] R. Sordella, D.W. Bell, D.A. Haber, J. Settleman, Gefitinib-sensitizing EGFR mutations in lung cancer activate anti-apoptotic pathways, Science 305 (5687) (2004) 1163–1167.

[9] C.S. Tan, N.B. Kumarakulasinghe, Y.Q. Huang, Y.L.E. Ang, J.R. Choo, B.C. Goh, R. A. Soo, Third generation EGFR TKIs: current data and future directions, Mol. Cancer 17 (1) (2018) 29.

[10] G. Goss, C.M. Tsai, F.A. Shepherd, L. Bazhenova, J.S. Lee, G.C. Chang, L. Crino, M. Satouchi, Q. Chu, T. Hida, J.Y. Han, O. Juan, F. Dunphy, M. Nishio, J.H. Kang, M. Majem, H. Mann, M. Cantarini, S. Ghiorghiu, T. Mitsudomi, Osimertinib for pretreated EGFR Thr790Met-positive advanced non-small-cell lung cancer (AURA2): a multicentre, open-label, single-arm, phase 2 study, Lancet Oncol. 17 (12) (2016) 1643–1652.

[11] J. Remon, C.E. Steuer, S.S. Ramalingam, E. Felip, Osimertinib and other third-generation EGFR TKI in EGFR-mutant NSCLC patients, Ann. Oncol. 29 (suppl_1) (2018) i20–i27.

[12] J. He, Z. Huang, L. Han, Y. Gong, C. Xie, Mechanisms and management of 3rd-generation EGFR-TKI resistance in advanced non-small cell lung cancer (Review), Int. J. Oncol. 59 (5) (2021) 90.

[13] L. Yi, J. Fan, R. Qian, P. Luo, J. Zhang, Efficacy and safety of osimertinib in treating EGFR-mutated advanced NSCLC: a meta-analysis, Int. J. Cancer 145 (1) (2019) 284–294.

[14] G.D.M. Veerman, K.G.A.M. Hussaarts, F.G.A. Jansman, S.W.L. Koolen, R.W.F. van Leeuwen, R.H.J. Mathijssen, Clinical implications of food-drug interactions with small-molecule kinase inhibitors, Lancet Oncol. 21 (5) (2020) e265–e279.

[15] D. Planchard, K.H. Brown, D.W. Kim, S.W. Kim, Y. Ohe, E. Felip, P. Leese, M. Cantarini, K. Vishwanathan, P.A. Jänne, M. Ranson, P.A. Dickinson, Osimertinib Western and Asian clinical pharmacokinetics in patients and healthy volunteers: implications for formulation, dose, and dosing frequency in pivotal clinical studies, Cancer Chemother. Pharmacol 77 (4) (2016) 767–776.

[16] S. Mura, J. Nicolas, P. Couvreur, Stimuli-responsive nanocarriers for drug delivery, Nat. Mater. 12 (11) (2013) 991–1003.

[17] Z.Y. Cao, D.D. Li, L. Zhao, M.T. Liu, P.Y. Ma, Y.L. Luo, X.Z. Yang, Bioorthogonal in situ assembly of nanomedicines as drug depots for extracellular drug delivery, Nat. Commun. 13 (1) (2022) 2038.

[18] E. Blanco, H. Shen, M. Ferrari, Principles of nanoparticle design for overcoming biological barriers to drug delivery, Nat. Biotechnol. 33 (9) (2015) 941–951.

[19] F. Danhier, O. Feron, V. Preat, To exploit the tumor microenvironment: passive and active tumor targeting of nanocarriers for anti-cancer drug delivery, J. Contr. Release 148 (2) (2010) 135–146.

[20] X. Li, Z.J. Ouyang, H.L. Li, C.L. Hu, P. Saha, L.X. Xing, X.Y. Shi, A. Pich, Dendrimer-decorated nanogels: efficient nanocarriers for biodistribution in vivo and chemotherapy of ovarian carcinoma, Bioact. Mater. 6 (10) (2021) 3244–3253.

[21] T. Su, X. Liu, S.B. Lin, F.R. Cheng, G.Z. Zhu, Ionizable polymeric nanocarriers for the codelivery of bi-adjuvant and neoantigens in combination tumor immunotherapy, Bioact. Mater. 26 (2023) 169–180.

[22] Y.Q. Zhu, Y.H. Song, Z.Y. Cao, L. Dong, S. Shen, Y. Lu, X.Z. Yang, A magnetically driven amoeba-like nanorobot for whole-process active drug transport, Adc. Sci. (2023), 2204793.

[23] R.S. Riley, C.H. June, R. Langer, M.J. Mitchell, Delivery technologies for cancer immunotherapy, Nat. Rev. Drug Discov. 18 (3) (2019) 175–196.

[24] R. Liu, C. Luo, Z. Pang, J. Zhang, S. Ruan, M. Wu, L. Wang, T. Sun, N. Li, L. Han, J. Shi, Y. Huang, W. Guo, S. Peng, W. Zhou, H. Gao, Advances of nanoparticles as drug delivery systems for disease diagnosis and treatment, Chin. Chem. Lett. 34 (2) (2022), 107518.

[25] H. He, L. Liu, E.E. Morin, M. Liu, A. Schwendeman, Survey of clinical translation of cancer nanomedicines-lessons learned from successes and failures, Accounts Chem. Res. 52 (9) (2019) 2445–2461.

[26] R.H. Fang, A.V. Kroll, W. Gao, L. Zhang, Cell membrane coating nanotechnology, Adv. Mater. 30 (23) (2008), 1706759.

[27] Y. Han, C. Gao, H. Wang, J. Sun, M. Liang, Y. Feng, Q. Liu, S. Fu, L. Cui, C. Gao, Y. Li, Y. Yang, B. Sun, Macrophage membrane-coated nanocarriers Co-Modified by RVG29 and TPP improve brain neuronal mitochondria-targeting and therapeutic efficacy in Alzheimer's disease mice, Bioact. Mater. 6 (2) (2020) 529–542.

[28] H. Liu, Z.H. Miao, Z.B. Zha, Cell membrane-coated nanoparticles for immunotherapy, Chin. Chem. Lett. 33 (4) (2022) 1673–1680.

[29] R.H. Fang, C.M. Hu, B.T. Luk, W. Gao, J.A. Copp, Y. Tai, D.E. O'Connor, L. Zhang, Cancer cell membrane-coated nanoparticles for anticancer vaccination and drug delivery, Nano Lett. 14 (4) (2014) 2181–2188.

[30] X. Liu, X. Zhong, C. Li, Challenges in cell membrane-camouflaged drug delivery systems: development strategies and future prospects, Chin. Chem. Lett. 32 (8) (2021) 2347–2358.

[31] Z. Cao, L. Feng, G. Zhang, J. Wang, S. Shen, D. Li, X. Yang, Semiconducting polymer-based nanoparticles with strong absorbance in NIR-II window for in vivo photothermal therapy and photoacoustic imaging, Biomaterials 155 (2018) 103–111.

[32] D. Li, Y. Ma, J. Du, W. Tao, X. Du, X. Yang, J. Wang, Tumor acidity/NIR controlled interaction of transformable nanoparticle with biological systems for cancer therapy, Nano Lett. 17 (5) (2017) 2871–2878.

[33] X. Sun, Y. Wang, K. Ji, Y. Liu, Y. Kong, S. Nie, N. Li, J. Hao, Y. Xie, C. Xu, L. Du, Q. Liu, NRF2 preserves genomic integrity by facilitating ATR activation and G2 cell cycle arrest, Nucleic Acids Res. 48 (16) (2020) 9109–9123.

[34] S.E. Ruff, S.K. Logan, M.J. Garabedian, T.T. Huang, Roles for MDC1 in cancer development and treatment, DNA Repair 95 (2020), 102948.

[35] I. Salguero, R. Belotserkovskaya, J. Coates, M. Sczaniecka-Clift, M. Demir, S. Jhujh, M.D. Wilson, S.P. Jackson, MDC1 PST-repeat region promotes histone H2AX-independent chromatin association and DNA damage tolerance, Nat. Commun. 10 (2019) 5191.